Materials & Design 220 (2022) 110898

Contents lists available at ScienceDirect

Materials & Design

journal homepage: www.elsevier.com/locate/matdes

Microstructural evaluation of sputtered Ru–Pt multilayer anti-stick coatings for glass molding

Awais Akhtar [a], Jianbiao Wang [a,b], Ruizheng He [b], Evans Yi Chun Wong [b], Karl Hung [b], Haihui Ruan [a,*]

[a] Department of Mechanical Engineering, The Hong Kong Polytechnic University Hung Hom, Kowloon, Hong Kong, China
[b] Biel Crystal Manufactory (Huizhou) Ltd., Huizhou, China

HIGHLIGHTS

- Ru and Pt monolayers, and Ru-Pt multilayer coatings were evaluated for precision glass molding.
- Multilayer coatings revealed better surface quality and anti-sticking performances than monolayer coatings.
- Hindrance in dislocation movement and atomic diffusion was explained by the addition of interfaces, and perseverance of multilayer structure was observed after long-term annealing.
- The performance of multilayer coatings was also validated by industrial testing.

GRAPHICAL ABSTRACT

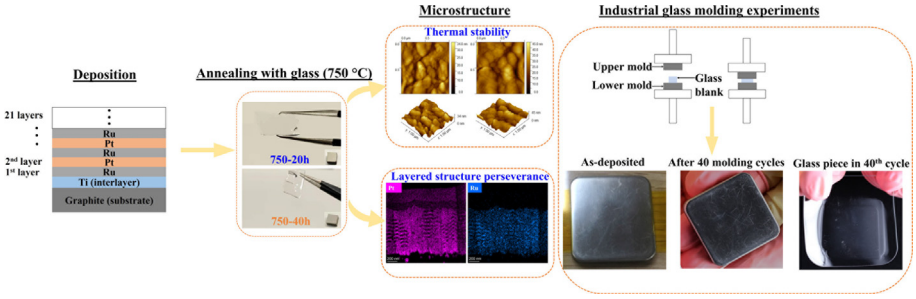

ARTICLE INFO

Article history:
Received 16 March 2022
Revised 4 June 2022
Accepted 24 June 2022
Available online 29 June 2022

Keywords:
Precision glass molding (PGM)
Anti-sticking performance
High-temperature stability
Multilayer coatings
Graphite substrate

ABSTRACT

This work describes the performance of multilayer Ru–Pt coatings with Ti as the interlayer deposited on graphite substrate for applications in precision glass molding (PGM). Different from the previous evaluations with other kinds of coatings for PGM temperatures below 650 °C, we studied the anti-sticking behavior of the developed coatings by annealing them at 750 °C with aluminosilicate glass coverage in a rough vacuum environment. Glass adhesion was not observed even after 40-hour annealing suggesting the high chemical inertness of the coatings at the high temperature. In addition, the Ru–Pt multilayer coatings exhibited a better anti-sticking property than monolayer (Ru or Pt) coatings. The microstructure, surface morphology, and hardness were further characterized. High-resolution transmission electron microscopy (HRTEM) analysis confirmed the perseverance of layered structure after annealing at 750 °C and the hindrance effect on dislocation motion and diffusion arising from the Ru-Pt interfaces. After long-term annealing, interdiffusion leads to Pt-Ru solid solutions, which further enhance the mechanical performance and stability of the noble metal coatings, beneficial for prolonging the lifespan of PGM molds and the optical quality of molded glass. The high anti-sticking and mechanical performances of the developed coatings were finally confirmed in industrial tests.

1. Introduction

Precision glass components with complex surface profiles or features are at the core of advanced optics in numerous applica-

* Corresponding author.
E-mail address: hhruan@polyu.edu.hk (H. Ruan).

https://doi.org/10.1016/j.matdes.2022.110898
0264-1275/

tions, including consumer electronics, laser technology, and medical technology [1,2]. To produce such glass parts in high volume, precision glass molding (PGM) is widely employed [3,4]. In PGM, the glass-mold adhesion must be inhibited to ensure high quality and polish-free glass surfaces; it endows PGM exceptionally cost-effective in mass production compared with the conventional grinding-polishing process. However, such a requirement is uneasy to meet. In PGM, mold surfaces experience severe cyclic thermo-mechanical loadings in contact with a softened glass workpiece at temperatures above its glass transition temperature (T_g) [5]; the occurrence of adhesion and even chemical reaction between contact surfaces results in premature mold failure, imperfections in molded glass surfaces, and the loss of dimensional control. Thus, the improvement of the inertness of mold surfaces at high temperatures draws research attention [6–8].

For PGM, tungsten carbide (WC) is regarded as an appropriate mold material owing to its high hardness, thermal stability, and wide availability. However, diamond turning must be employed for machining such a hard and brittle material, making WC molds extremely costly and time-consuming to fabricate [9]. In addition, it possesses a tendency to react with glass because tungsten and binder materials (e.g., Co) are active at elevated temperatures [10,11]. Hence, WC molds must be coated with inert materials to prolong their service life. It is noted that the literature of the coatings on WC substrate for PGM explores the anti-sticking and mechanical performance under the molding temperatures below 650 °C [10,12] probably because most optical glass, essentially borosilicate glasses (BSGs), can be molded below it.

However, the challenge encountered is to thermoform aluminosilicate glasses (ASGs) that are ubiquitously used as screen covers and will find further applications in virtual/augmented reality (VR/AR) glasses and smart vehicles. The molding temperatures for ASGs must be in the range of 700 – 800 °C, which is an unattempted temperature range for PGM coatings. WC molds become even more costly to use in this higher temperature range because of the significantly reduced tooling life, the consequence of enhanced diffusivity and reactivity of active elements. Hence, graphite is more used owing to its thermal stability and, more importantly, excellent machinability [13] because the latter gives rise to the low manufacturing cost in production trials for compensating form errors. However, graphite is low-strength and brittle, thermo-mechanical loading and glass sticking in a molding process quickly damage the surfaces of graphite molds, leading to the adherence of graphite powders on molded glass surfaces. These glass surfaces must be ground and polished, making the graphite-based molding no longer high-precision and cost-effective; that is, graphite-based glass molding is no longer a PGM process.

Hence, the technical question in this work is whether graphite-based glass molding can still reach a high precision if appropriate protective coatings are used. The essential requirements for such surface coating are (1) superior thermal stability, (2) high hardness with sufficient thermal-shock resistance, (3) high chemical inertness with glass elements. With this question, let us briefly review the recent investigations of PGM coatings.

In a nutshell, PGM coatings can be classified into three types, namely, diamond-like carbon (DLC) coatings [14], ceramic coatings (*e.g.*, TaN, TiAlN, CrWN) [6,15,16], and noble metal coatings [17–19]. Although DLC coatings have excellent anti-wear and self-lubrication performances at low temperatures, their poor thermal stability (transform to graphite at temperatures over 600 °C) and high fabrication cost (requiring special facility) restrict the application for PGM in the glass industry [20,21]. Ceramic coatings demonstrated better thermal stability than DLC coatings. However, at temperatures higher than 500 °C [22], oxidation of metallic elements occurs easily, resulting in glass adhesion and coating deterioration. Noble metal coatings are considered to be the most reliable for PGM and have been widely utilized industrially due to their superior resistance to corrosion and oxidation and high operating temperatures (typically 600 – 700 °C) [11]. Noble metals such as platinum (Pt), iridium (Ir), and rhenium (Re) were widely studied in the past years for PGM application. Among them, the Pt–Ir coating system is the most employed because of its high oxidation and corrosion resistance and excellent anti-sticking performance.

However, for high–T_g glasses (e.g., ASGs), noble metal coatings may still suffer from oxidation and sticking problems when T greater than 700 °C. Furthermore, Ir is three to four times more expansive than Pt, making the glass industry daunting to employ. Thus, new coating systems must be explored to address these challenges. In the noble metal group, ruthenium (Ru) is a low-cost (around 1/3 cheaper than Pt) and highly inert element. The oxidation resistance of Ru is even higher than that of other noble metals, such as Pt and Ir [23]. Chen et al. [24] developed MoRu coatings on WC substrates; after annealing at 600 °C, they observed that coatings with the higher Ru content (at least higher than Mo content) exhibited superior oxidation resistance and higher hardness. These results indicate that Ru can be a coating material for PGM when an increase in chemical inertness is required, especially when high-T_g glasses are subjected to molding. Nonetheless, pure Ru is brittle owing to the HCP structure; hence a ductile noble metal, such as Pt, may be involved in the coatings. It is noted that the Ru-Pt system has been employed for electrocatalysis [25] and for making contact electrodes [26], owing to its superior oxidation and corrosion resistance. Following these practices, a multilayer Ru–Pt coating with titanium (Ti) interlayer was developed on graphite substrates by the magnetron sputtering technique. The anti-sticking performance of the coating was evaluated by annealing coated samples with ASG coverage. In addition, phase stability, microstructural evolution, and mechanical properties of the Ru–Pt multilayer coatings were examined. Based on these characterizations, enhancement in mechanical and anti-sticking performances, in comparison with monolayer (Ru or Pt) coatings, were explained.

2. Materials and methods

A magnetron sputtering system (Denton Explorer 14 Sputtering System) was employed for the deposition of thin films. Pure Ru, Pt, and Ti disks with diameters of 50.8 mm, 50.8 mm, and 76.2 mm, respectively, were utilized as the sputtering targets with constant substrate-to-target distance in the vacuum chamber. The substrates were graphite cubes with a side length of 5 mm, which were initially ground and polished by applying diamond paste to achieve ultrasmooth surfaces (roughness Ra < 10 nm). Before the deposition process, the vacuum chamber was pumped down to 8×10^{-7} torr followed by argon (Ar) gas inlet as plasma source. Ar flow rate was maintained at 30 sccm, and all the targets were pre-sputtered to obtain clean target surfaces. Ti interlayer of 50 nm thickness was deposited on the graphite substrates to improve adhesion between protective coating and substrate. Multilayer Ru–Pt coatings were accomplished by alternative deposition of Ru and Pt layers, each with a thickness of 40 nm. The total number of deposited layers were 21, starting and ending with Ru (Ru–Pt–Ru–Pt–Ru...Pt–Ru); thus, the total thickness of the multilayer coating was 840 nm. The monolayer Ru or Pt coatings with a thickness of 840 nm were deposited on substrates with 80 W input power as the control samples.

To investigate the chemical inertness of the developed coatings, an ASG piece (Corning Gorilla glass 5, $T_g \approx 630$ °C) was positioned on the coated samples and heated in a quartz tube furnace under a rough vacuum (~1 mbar) condition. Annealing involved the rise in

temperature with a heating rate of 5 °C/min from room temperature to 750 °C and soaking for 2, 20, and 40 h, respectively. Afterwards, annealed samples were cooled down in the tube furnace to room temperature. The as-deposited and annealed samples at 750 °C for 2, 20, and 40 h are designated as AD, 750–2 h, 750–20 h, and 750–40 h, respectively.

X-ray diffractometer (Rigaku SmartLab) with Cu-Kα radiation was employed to investigate the crystallinity of the developed coatings before and after annealing. The Cu-Kα radiation was produced from copper anode operated at 45 kV and 200 mA. The surface morphologies and surface roughness were evaluated by scanning electron microscopy (SEM-TESCAN VEGA3) and scanning probe microscopy (SPM-Bruker Nasoscope 8), respectively. Nanoindentation tests were performed on all the Ru-Pt coated samples to determine the mechanical properties, such as hardness (H) and Young's modulus (E) using Berkovich indenter (Hysitron Nanoindentation system). A load of 250 μN was used for all the samples, and thus, the penetration depth was not exceeded above 10% of the overall coating thickness in order to avoid the substrate effect. The chemical binding of multilayer coatings was examined by X-ray photoelectron spectroscopy (XPS, Thermo Scientific Nexsa). The nanostructure of the multilayered coatings was examined by scanning/transmission electron microscope (S/TEM, FEI Talos 200X) operated under a 200-kV accelerating voltage. A dual-beam focused ion beam (FIB) equipped with ultrahigh electron beams and ion beams were employed to prepare cross-sectional TEM specimens. Before ion-beam cutting, the Pt protection layer was deposited to the specific surface area of the sample by using electron-beam (e-beam) deposition at 2 kV and then ion-beam deposition at 30 kV. Then the sample is deeply trenched in the Pt-coated area by the gallium ion beams. Following that, the TEM micro-sample was extracted from the bulk sample, lifted out using a micromanipulator, and then transferred and welded to a TEM sample mount. Further thinning of the lamella was conducted with FIB milling to achieve electron transparency (<100 nm). Ru-Pt multilayer coatings were also deposited on larger graphite (~40 × 40 mm) plates, which were subsequently used to press ASG using an industrial glass molding system with an N_2-flowing environment to investigate the performance of the developed coatings in the harsher environment.

3. Results and discussion

3.1. Phase identification

Fig. 1(a) shows the photographs of the coatings in the as-deposited and annealed states. Visually, the annealed coatings (750–20 h and 750–40 h) remained almost identical to the as-deposited one (i.e., no delamination, color change, or surface contamination), and the glass pieces used as the coverage in annealing remained fully transparent. Fig. 1(b) shows the XRD patterns of the substrate and the Ru–Pt coated samples before and after annealing. These patterns exhibit a similar set of peaks before and after annealing, signified by the reflections of Ru (HCP), Pt (FCC), Ti (HCP), and graphite substrates. In the as-deposited coatings, primary diffraction peaks of Pt and Ru located at 39.7° and 42.2° correspond to the preferred orientation of (111) and (002) planes, respectively. After two hours of annealing at 750 °C, annealed coatings maintained the stable structure of Pt and Ru phases except that the diffraction peak of Pt (111) slightly shifted towards the higher angles corresponding to a lattice expansion. Such a result is similar to those reported in ref. [27,28], which is likely due to a decrease in compressive residual stress. With continuous annealing for 20 h and 40 h, the Pt (111) diffraction peak became narrower and more intensified but no longer shifted, whereas the Ru (002) weak peak shifted slightly towards lower angles. The Pt (111) and Ru (002) peaks can be utilized to estimate the average crystallite sizes. The crystallite sizes of the Pt and Ru in the as-deposited and annealed state were calculated by using Scherrer's equation [29].

$$D = \frac{k\lambda}{\beta \mathrm{Cos}\theta} \tag{1}$$

where D is the average crystallite size, k is a constant (0.94), λ the X-ray wavelength (1.54 Å for CuKα), θ the Bragg angle pertaining to a peak, and β the full width at half maxima (FWHM). Thus, the crystallite size was calculated to be 9.7 and 16.9 nm for Pt and Ru in the as-deposited state, respectively, and 17.2 and 8.2 nm for Pt and Ru in the 40-hour annealed state, respectively. It is noted that the Pt crystallite size increased after annealing, whereas, for Ru, annealing led to a decrease in crystallite size, indicating grain refinement. This grain refinement can be ascribed to the twinning induced grain subdivision, which will be exhibited by TEM results.

3.2. Surface morphology and roughness studies

Surface morphologies of Ru–Pt multilayer coatings evaluated by SEM are exhibited in Fig. 2. It is observed that the DC sputtering resulted in the continuous, dense, and coarse surface morphology (Fig. 2(a)). The associated energy-dispersive x-ray spectroscopy (EDS) analyses showed reflections of Ru and Pt. As the sampling depth of EDS is in the micrometres range [30], larger than the overall coating thickness, reflections of carbon from the substrate were also recorded, as depicted in Fig. 2(b). It is observed that the Pt and Ru grains become slightly more spherical after prolonged annealing (Fig. 2(e, g)). No surface cracks were observed on the multilayer-coated samples. The surface morphologies of 840 nm monolayer Ru and Pt coated samples before and after 2 h annealing at 750 °C are exhibited in Fig. 3. A few micro-cracks on the Pt surface without annealing were observed (Fig. 3(a)). After 2 h annealing with glass coverage, cracks become much more significant in the Pt coated surface (Fig. 3b). This could possibly be owing to the lattice mismatch between Ti/Pt and graphite substrate, which resulted in the coating deterioration and, therefore, slight glass adhesion or chemical reaction between glass/coating. The inset in Fig. 3(a) shows the schematic of the heteroepitaxial interface: Ti {101} || Pt {111}, which are determined based on the corresponding XRD pattern. Note that when Ti is deposited on graphite, it has FCC structure owing to the formation of TiC [31]. The crystal lattice mismatch leads to the changes in lattice constants, which can be manifested by the XRD peak shift (0.53° for Pt {111} and −0.41° for Ti {101}). The mismatch results in the accumulation of strain energy, causing irreversible deformation and defects, such as pores and cracks, in the monolayer coating. During deposition, cracks have already propagated to the Pt surface as shown in Fig. 3(a). After the short-term annealing, cracks become more significant as shown in Fig. 3(b).For the Ru monolayer coating, no glass adhesion was observed, and a fairly smooth surface is exhibited after 2 h annealing (Fig. 3(d)). Owing to the inherent brittleness of Ru, a few micro-cracks appeared after 2 h annealing.

In contrast to Ru and Pt monolayers, better surface quality and anti-sticking properties were exhibited by the Ru–Pt multilayer structure, which could be ascribed to the interfaces that inhibit the atomic diffusion on both sides (glass and substrate) [12]. In addition, the thin and ductile Pt layers kept Ru from cracking during annealing. Fig. 4(a-d) displays the SEM images of top surfaces of Ru–Pt multilayer coatings before and after annealing. These coated samples exhibited very smooth and uniform surfaces even after 40 h annealing. The average particle size of the coatings was calculated from the SEM images by selecting isolated particles

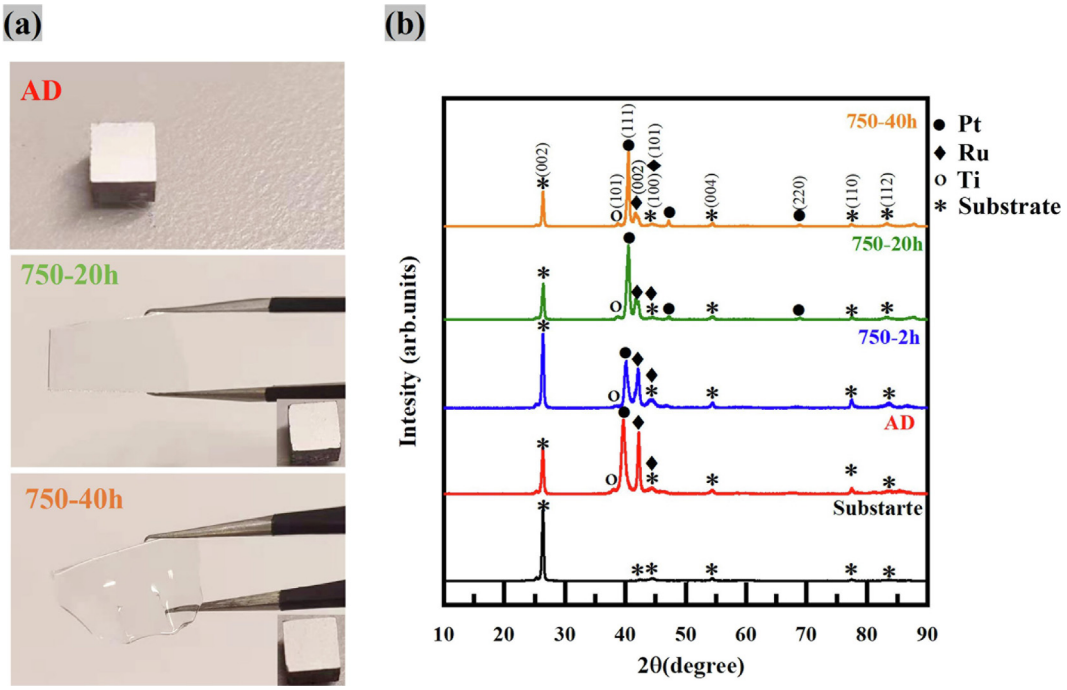

Fig. 1. Coated and annealed samples: (a) photographs of AD, 750–20 h and 750–40 h coated samples with their covering glass pieces in annealing and (b) XRD patterns of the substrate and of Ru–Pt multilayer coatings (AD, 750–2 h,750–20 h,750–40 h).

using the Image J software. In Fig. 4(e-h), the histogram reveals the particle size distribution of the as-deposited and heat-treated multilayer coatings. The average particle sizes of AD, 750–2 h, 750–20 h, and 750–40 h samples were 0.35, 0.36, 0.36, and 0.39 μm, respectively. The statistical results of Ru-Pt multilayer coatings are summarized in Fig. 4(e-h) and Table 1. It is observed that the particles become slightly coarsened after annealing for a long time, but the increase in surface particle size is insignificant. It is noted that the average surface particle size is larger than the average grain size determined from XRD patterns. The reason is that the surface particles may be agglomerations of grains with different orientations, which form spherical shapes to minimize surface/interface energy.

The morphologies of coating surfaces were further characterized by AFM, as shown in Fig. 5. The scanning area of each image was set to $1 \times 1\ \mu m^2$. All of the AFM images exhibited dense and granular structure morphology with visible agglomerated grains. The AFM 3D images confirmed the crack-free surfaces. The average surface roughness (R_a) and root mean square roughness (R_q) of the as-deposited coatings were 16.37 nm and 21.33 nm, respectively. For 2 h, 20 h, and 40 h annealed samples, R_a/R_q values were 18.86/19.11, 19.39/22.07, and 24.57/25.03 nm, respectively. Apparently, the longer annealing facilitated the coalescence of adjacent particles, as shown in Fig. 5, resulting in an increase in roughness [32]. It is worth noting that the annealed coatings persisted with a smooth surface with a litter change of roughness after heating with glass coverage. Thereby, the observation of the surface morphology evolution leads to the assertion that the Ru–Pt multilayer coatings demonstrated significant thermal stability in terms of surface characteristics at 750 °C.

3.3. Mechanical properties and XPS analysis

Fig. 6 exhibits the typical curves of load versus penetration depth obtained by nanoindentation tests for the as-deposited and annealed Ru-Pt multilayer coatings. It can be observed that the maximum penetration depth was reduced for annealed coatings compared to as-deposited ones under the same load. The hardness and Young's modulus (H) and (E) were determined from the nanoindentation curves and are reported in Table 2, which illustrates significant increases in H and E with annealing time. The improvement in mechanical performance is primarily owing to the multilayer enhancement mechanism resulting from the dislocation blockage by the multilayer interfaces [12]. In heterostructure materials, crystallographic structures, slip plane orientations, and slip directions vary significantly across the interfaces. With lattice misfit strains, the stressed interfaces can further prohibit dislocations from crossing them. This is the case in our multilayer system, wherein the Pt-Ru interfaces act as stronger barriers to dislocation motion. The interfaces were originally wavy, which allows more directions for dislocations to glide. After the brief (two hours) annealing, interfaces became flattened (see the following TEM results), which confines dislocations to move mainly in the in-plane directions. Hence, a significant increase in hardness was observed. After the long (20 and 40 h) annealing time, it is observed that the hardness further increases, which could be attributed to the effect of solid-solution hardening caused by the interdiffusion of Pt and Ru to form their alloys. In addition, we did not observe a significant increase in grain size after the long-term annealing, probably caused by the constraint of layered structure; hence the softening caused by grain growth is insignificant.

The investigation of the surface chemical states was carried out by XPS. Fig. 7 (a, b, c) shows the XPS spectra of Ru 3d in the annealed states. After 2 h annealing, the Ru 3d spectra exhibited doublet of Ru $3d_{5/2}$ and Ru $3d_{3/2}$ with binding energies of 280.3 and 284.3 eV, which are in line with the reported values of pure metallic Ru [33]. After longer annealing, no noticeable change in the binding energies was observed for the Ru 3d doublet, indicating that the Ru sustained its metallic state. However, for the 750–40 h sample, Ru 3d spectra recorded only one peak of Ru ($Ru3d_{3/2}$ = 285.1 eV), which overlapped with the same energy region of C (C1s = 285.1 eV) [33]. Therefore, this peak could correspond to elemental carbon (C-C) bonds [34,35]. Fig. 7(d) demonstrates the two characteristic peaks of metallic Pt (Pt 4f

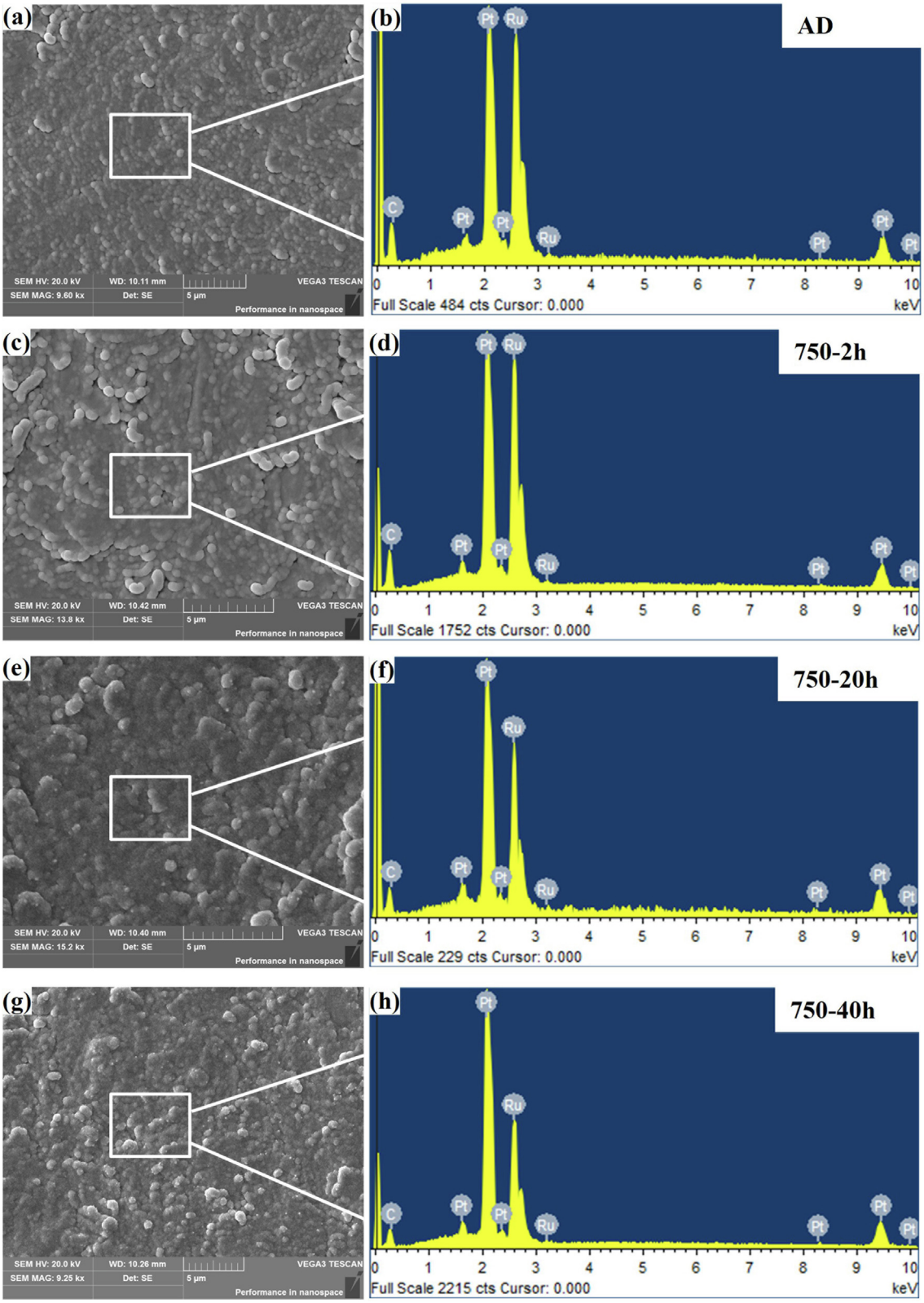

Fig. 2. SEM surface morphology and corresponding EDS spectrum of marked areas in SEM images of samples (a, b) AD, (c, d) 750–2 h, (e, f) 750–20 h and (g, h) 750–40 h.

$_{5/2}$ = 71.8 eV) and (Pt 4f $_{7/2}$ = 75.2), which are in good agreement with the reported values [36,37]. Furthermore, after 40 h annealing (Fig. 7(f)), the binding energy of Pt 4f shifted negatively by ca. 0.3–0.4 eV, revealing that the occurrence of charge transfer from Ru to Pt (owing to the higher electronegativity of Pt), indicating the interaction of Pt and Ru [38].

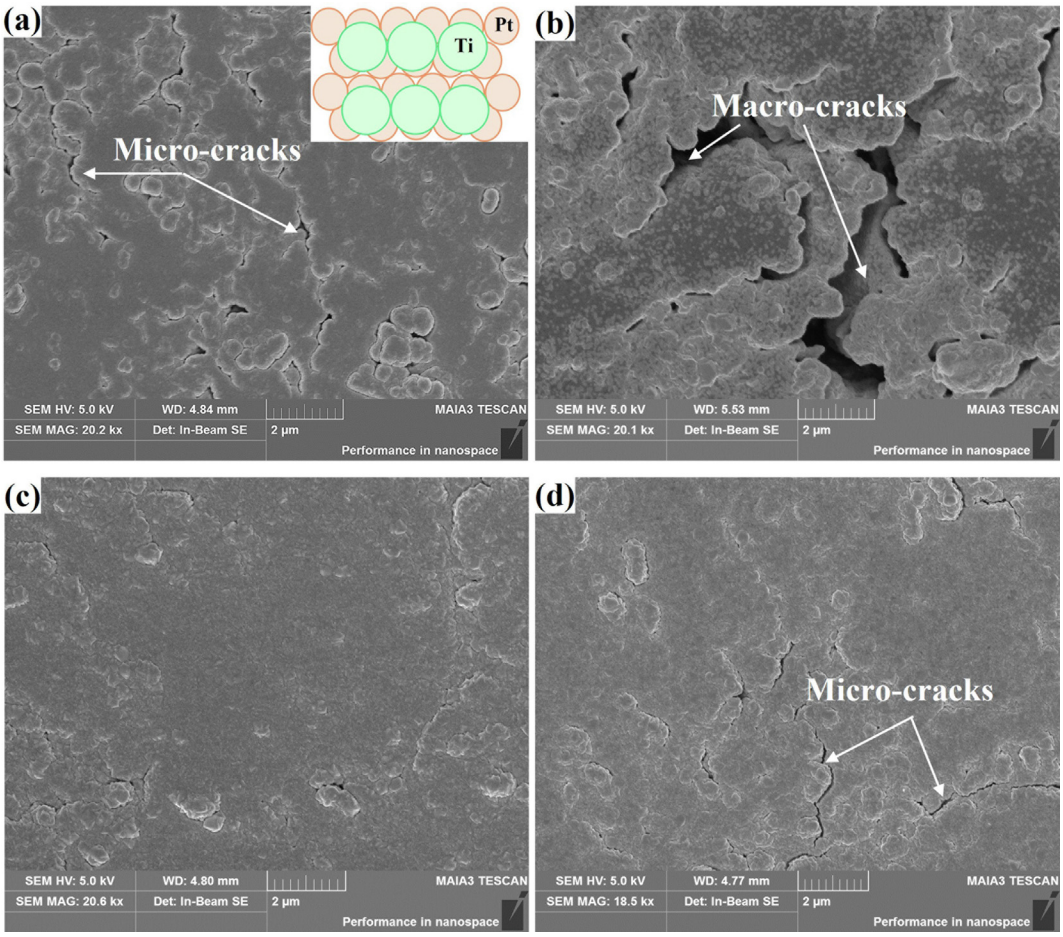

Fig. 3. Surface morphology of monolayers Pt (a,b) and Ru (c,d) in the as-deposited (a,c) and annealed state (b,d).

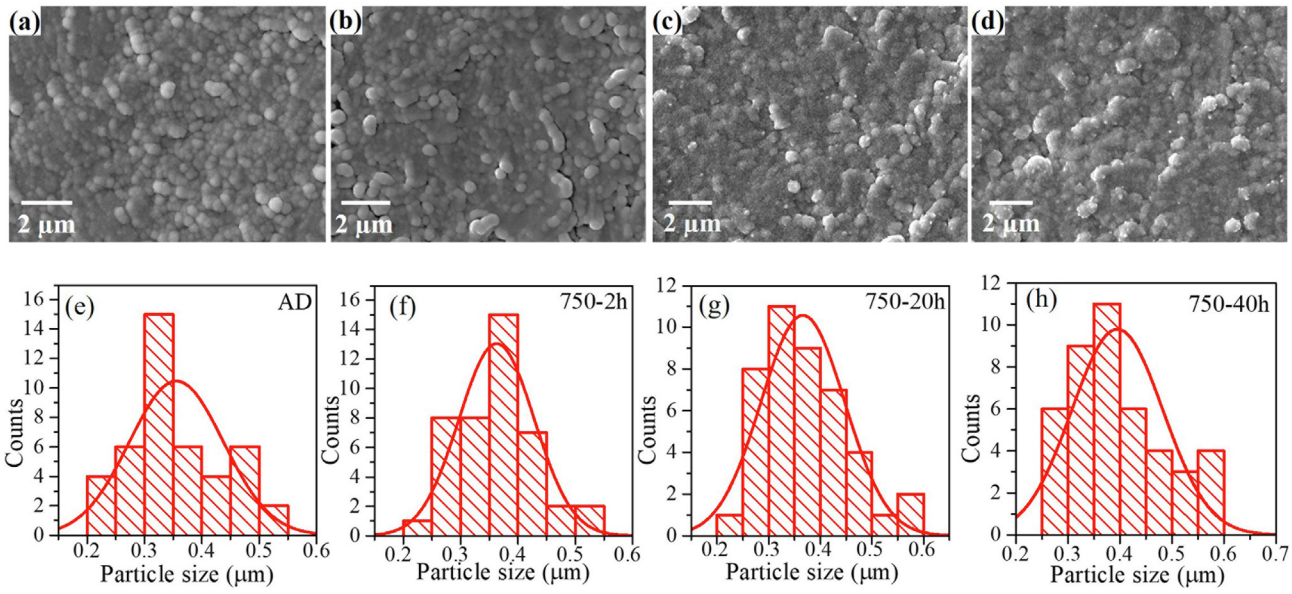

Fig. 4. SEM images and particle size distribution of as-deposited and annealed coated samples: (a, e) AD, (b, f) 750–2 h, (c, g) 750–20 h and (d, h) 750–40 h.

3.4. Microstructural evolution

Fig. 8 shows the typical TEM image of the cross-section of the as-deposited multilayer coatings. A homogeneous and dense cross-sectional morphology with a uniform nano-laminated structure can be observed. In Fig. 8, the alternating Ru and Pt layers, the Ti interlayer, and the graphite substrate can be clearly discerned. The sputtering process leads to the pseudo columnar structure per-

Table 1
Particle size distribution and average particle size of the Ru–Pt multilayer coatings.

Sample ID	Particle Size distribution (μm)	Average size (μm)
AD	0.22 – 0.52	0.35
750–2 h	0.23 – 0.51	0.36
750–20 h	0.20 – 0.55	0.36
750–40 h	0.27 – 0.59	0.39

pendicular to the substrate surface [39]. The dome-shaped columns resulted in the wavy structure of the nano-crystalline coating layers. Additionally, internal stresses (due to lattice mismatch or thermal effect) developed during the deposition could also induce waviness [40].

To get the structural insight, high-resolution transmission electron microscopy (HRTEM) was conducted at the interfacial area of Ru–Pt. Fig. 9(a) depicts the HRTEM image of the as-deposited multilayer coatings with an inset showing a corresponding selected area electron diffraction (SAED) pattern. The cross-sectional HRTEM image exhibited dense microstructure with no porosity, and a multi-ring pattern was observed in the SAED, confirming the nano-crystalline phases. The Inverse Fast Fourier Transform (IFFT) image of the as-deposited coatings is shown in Fig. 9(b). It is evident that the lattice distortion occurred at the interface owing to the dissimilar crystal lattice of Ru (HCP) and Pt (FCC). The misfit dislocations were recognized clearly and marked by the symbol "T" in the IFFT image. The wavy structure in the as-deposited state indicates the existence of compressive residual stresses. In the IFFT-TEM image, we observed dislocations formed at the interface. Furthermore, owing to the lattice mismatch between two layers, coherency strains and lattice distortion are also generated, and the blockage of dislocation at the interfaces eventually results in mechanical strengthening and impediment of atomic diffusion [12,41].

Fig. 10 shows the cross-sectional HRTEM images of 2 h annealed coatings. It is noted that the coated layers maintained laminated structure after the annealing, and the waviness of interfaces slightly mitigated during the annealing process (Fig. 10(a)). No amorphous phase was observed at the interface. Annealing at high temperatures induces hardening effects ascribed to the coherency strains. Dislocation movement is impeded by the coherency [42], as it is relatively more difficult for dislocation to pass through a strained lattice than an unstrained one. In the multilayer structure, interfaces already restrict the movement of dislocations; coherency strains further contribute to the hardness enhancement by making dislocations difficult to glide. Hence, we observed an increase in the nano-hardness in the nanoindentation experiments. Fig. 10(d) shows the SAED pattern taken from an area enclosing the Pt-Ru interface as indicated in Fig. 10(a). The spots in the SAED pattern confirm the nanocrystalline nature of the multilayered coatings. In addition, it is observed that after the short-term annealing, the multi-ring pattern (inset of Fig. 9(a)) is transformed into the pattern with many spots, which can be ascribed to the change in the grain sizes [43] and grain orientations. The latter could be associated with the flattened interfaces after the brief annealing.

Fig. 11 shows the high angle annular dark-field (HAADF) image and the EDS mapping acquired in the STEM mode. In HAADF-STEM, the dark gray and bright gray areas correspond to Ru and Pt (opposite those in HRTEM image) as confirmed by EDS mapping. In Fig. 11(b), the elemental mapping image, a layered structure can be clearly observed. Fig. 11(d) confirms that the annealed coatings (sample 750–2 h) sustained the multilayer structure, which indicates the thermal stability of the multilayer noble metal coatings after annealing at 750 °C for 2 h.

Figs. 9-11 illustrates the wavy interfaces in the as-deposited coatings and the reduction in waviness after a brief annealing. It is conceived that the wavy interface is caused by residual stresses in the as-deposited thin films. However, the residual stresses were not measured because of the difficulty to determine them in the nanolayers. Hence, let us explain the possible causes of them here. The primary contributions of residual stress in the thin films are intrinsic and thermal stresses, arising from the mismatches in the crystal structures and coefficients of thermal expansion (CTE), respectively. The intrinsic stresses, i.e., those arise from lattice misfit, is straightforward as the crystal structures across interfaces are disparate. The thermal stresses could be caused by the high kinetic energy of sputtered particles. They induced local heating and hence thermal effect. In addition, during deposition, residual stresses may also be caused by the effect of implantation (e.g., Ru atoms are squeezed into the Pt lattice). All these effects can be mitigated through dislocation motion and diffusion, which occurred during annealing. In particular, dislocation motion within nanolayers can be explained based on the confined layer slip (CLS) mechanism [44–47].

Based on the CLS mechanism, in a submicron or nanolayer lack of space for dislocation pile-up, dislocations are difficult to cross an

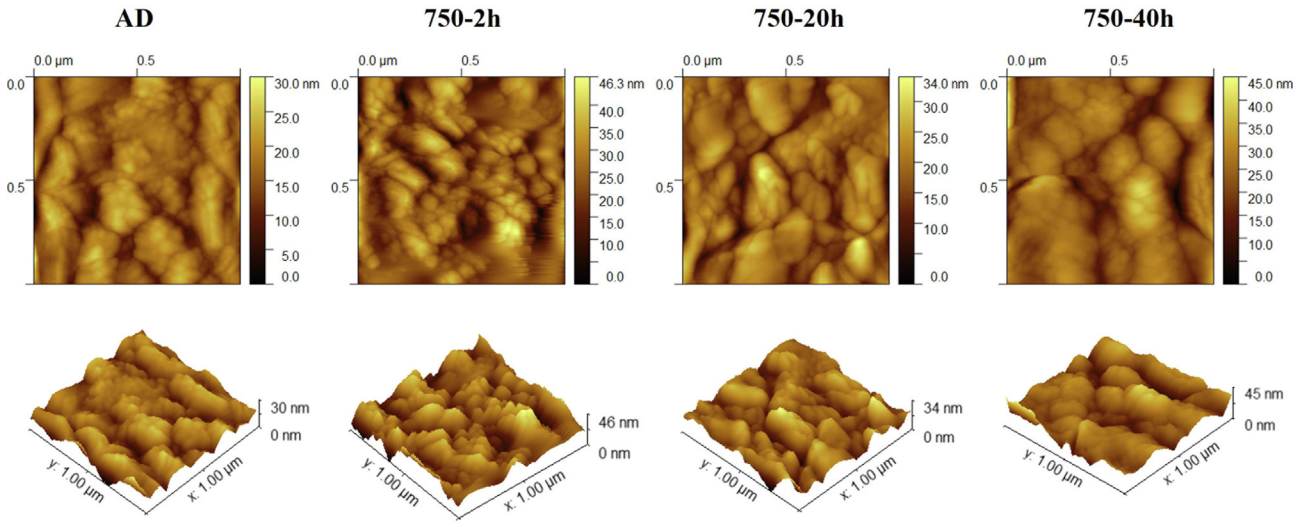

Fig. 5. AFM surface morphology (2D, 3D) of samples AD, 750–2 h, 750–20 and 750–40 h.

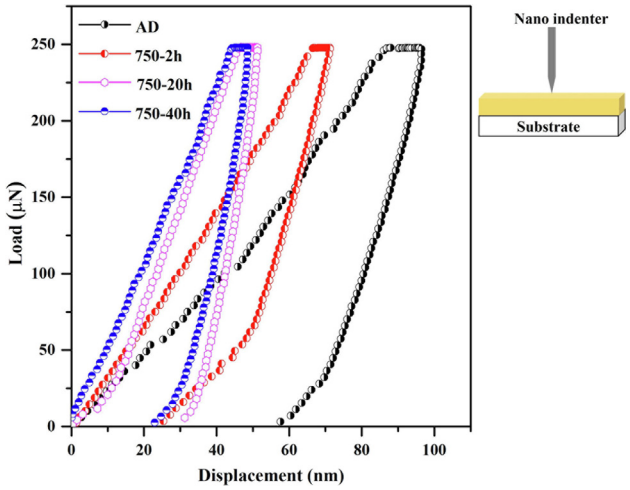

Fig. 6. Nanoindentation (load-depth) curves of the Ru–Pt multilayer coatings.

Table 2
Mechanical properties (H) and (E) of Ru–Pt multilayer coatings.

Sample ID	H (GPa)	E (GPa)
AD	1.14	18.99
750–2 h	2.06	28.52
750–20 h	3.15	59.48
750–40 h	3.61	59.50

interface and can only glide within a thin layer by bowing between the interfaces, which leaves misfit dislocations behind. The interaction of misfit dislocations with passing dislocations induces an increase in flow stress and strain hardening. When the thickness

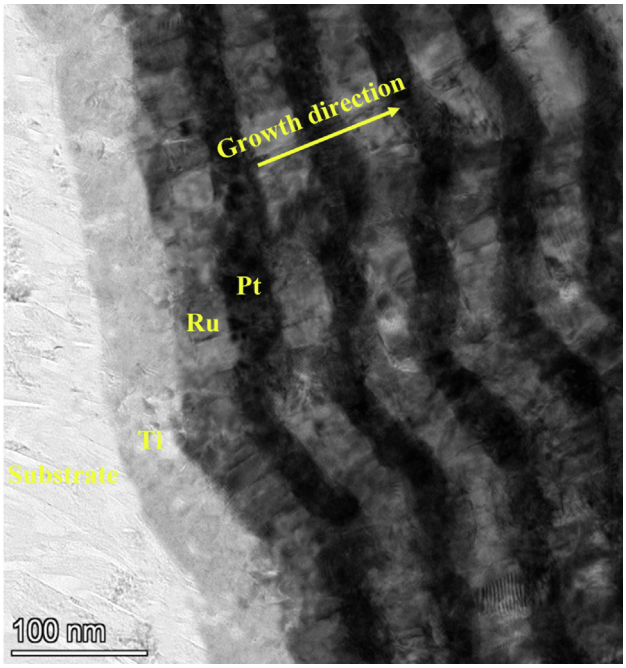

Fig. 8. Typical cross-sectional TEM image of the as-deposited multilayer coatings.

of the layers is in nanometers, such a confinement effect becomes very significant, i.e., dislocations are unable to bow. In this case, dislocation glide across the interface becomes the key mechanism in determining the strength. The more disparity in crystallographic structure across an interface leads to a higher barrier to dislocation transmission. With high interfacial barriers, gliding dislocations

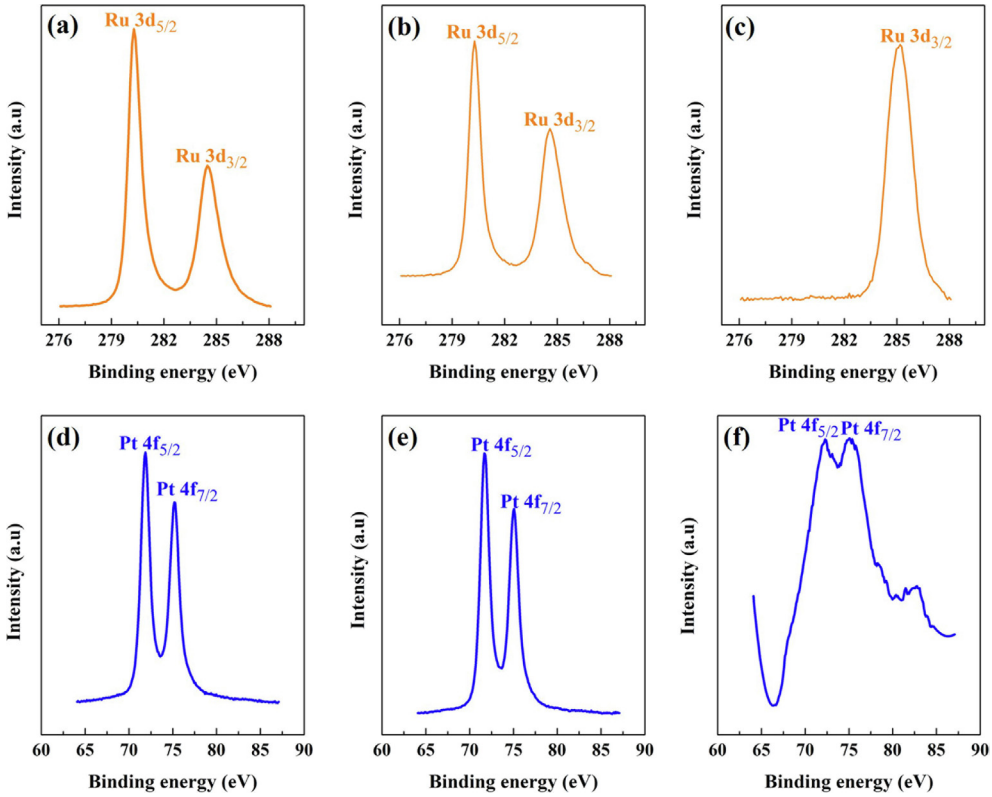

Fig. 7. XPS spectra of Ru 3d (a, b, c) and Pt 4f (d, e, f); (a, d) sample 750–2 h, (b, e) sample 750–20 h and (c, f) sample 750–40 h.

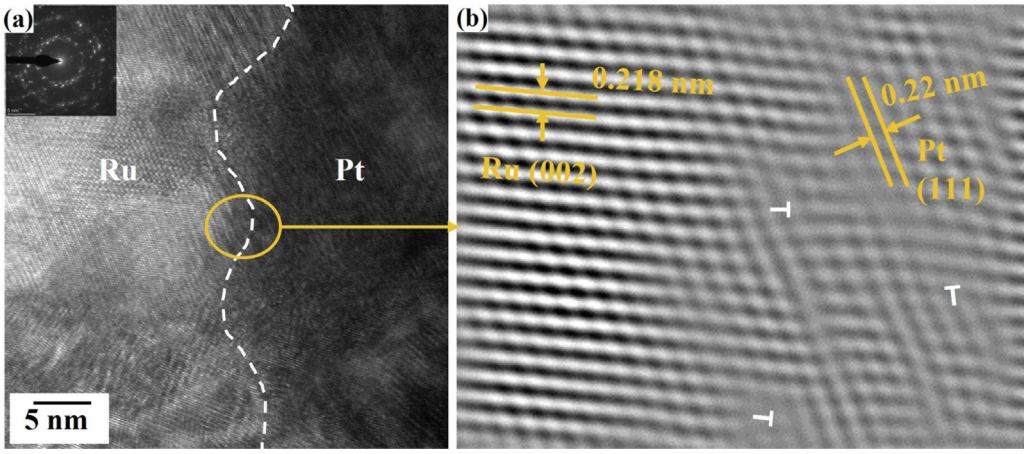

Fig. 9. As-deposited Ru–Pt multilayer coating images of (a) High-resolution transmission electron microscopy (HRTEM); and (b) Inverse Fast Fourier Transform (IFFT).

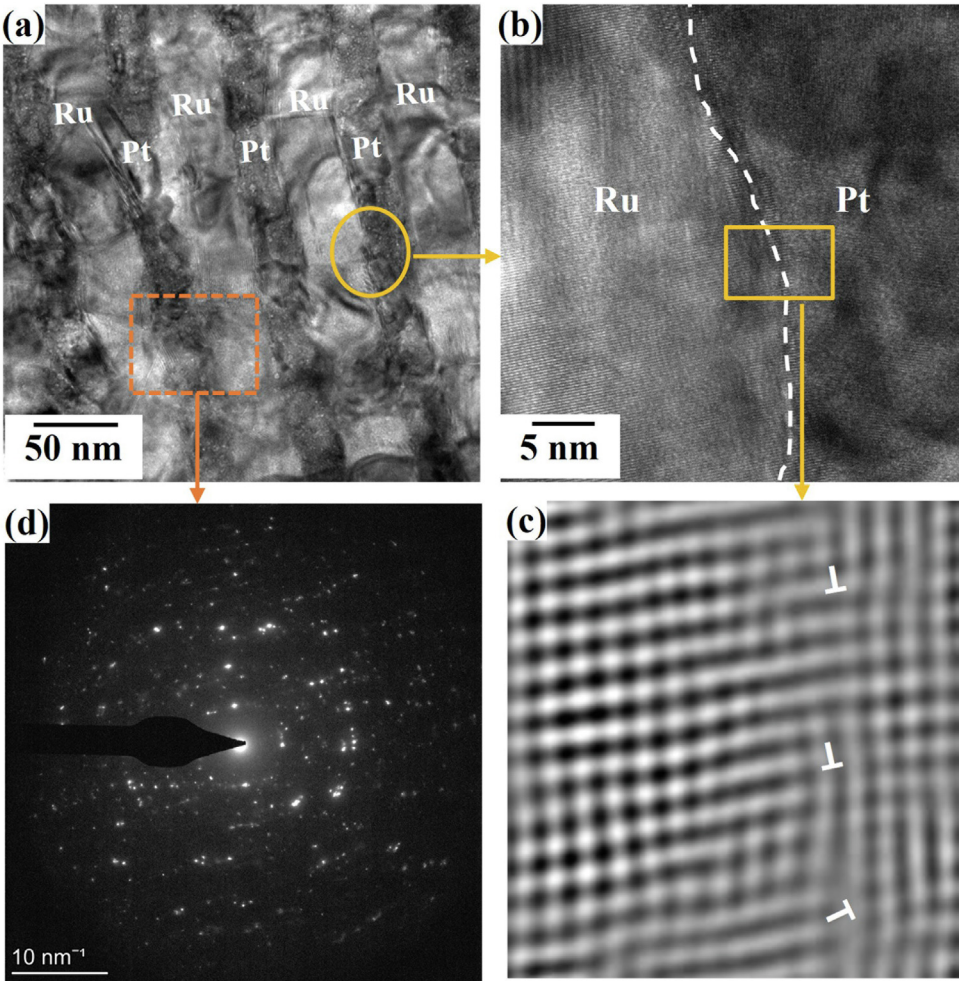

Fig. 10. HRTEM images and SAED patterns of annealed (750–2 h) coatings (a) cross-section, (b) Ru–Pt interfacial area marked in (a), (c) IFFT image of (b), (d) SAED pattern of marked area in (a).

are absorbed in interfaces by forming dislocated structures (i.e., dislocation cores) spreading along the interface plane. With this spreading process, resistance to dislocation gliding becomes stronger and the hardness increased after brief annealing.

Among different crystalline structures, HCP metals are very likely to have deformation twins upon straining owing to the lack of enough slip systems required for change in shape arbitrarily [48]. Twinning results in the shearing of specific crystallographic planes, forcing the atoms to relocate into an arrangement with a different orientation from the parent crystal. In the as-deposited coatings, twinning is not observed in the HRTEM results (i.e., no growth twins); however, annealing twins were observed, as exhibited in Fig. 12, in the annealed sample 750–40 h. This can explain the grain refinement in Ru layers as revealed by XRD analysis. In

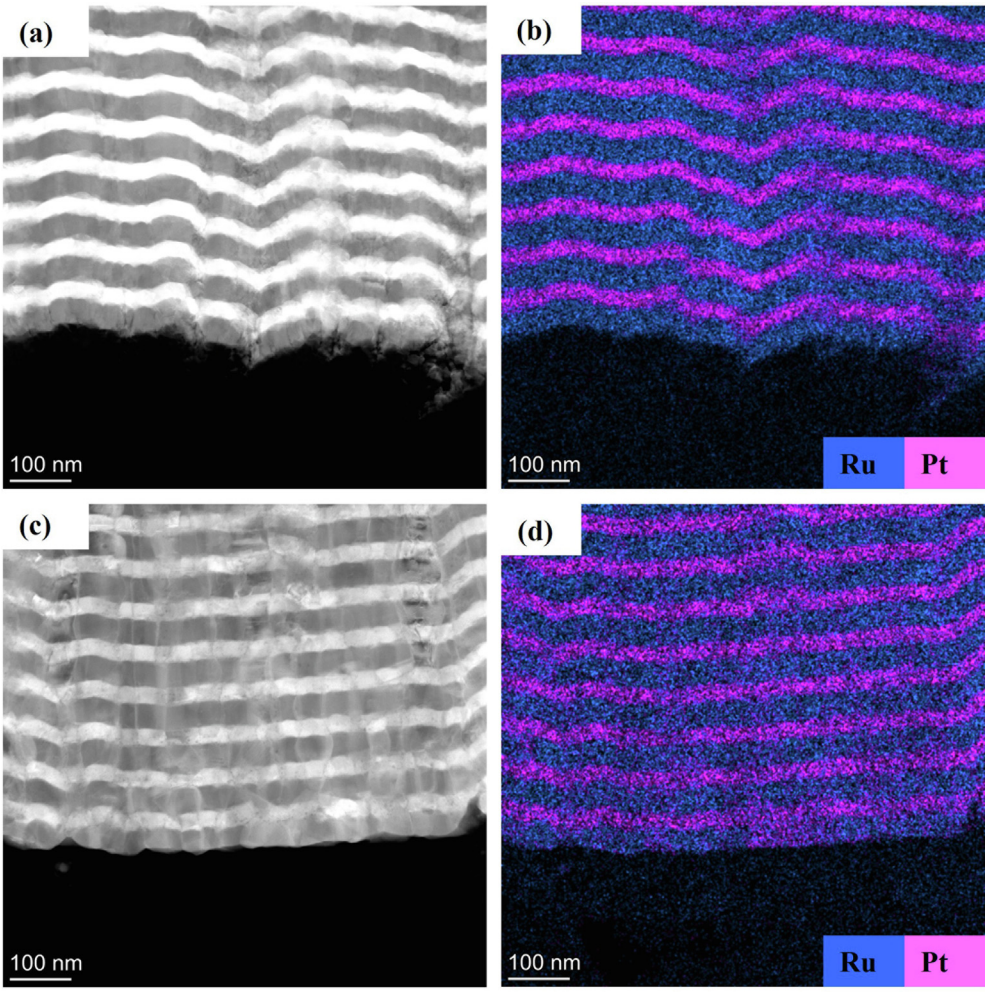

Fig. 11. HAADF-STEM images and EDS mappings. (a, b) cross-section of sample AD and (c, d) cross-section of sample 750–2 h.

addition, annealing twins contribute to the increase in hardness with annealing time because twin boundaries (TBs) efficaciously impede mobile dislocations [48].

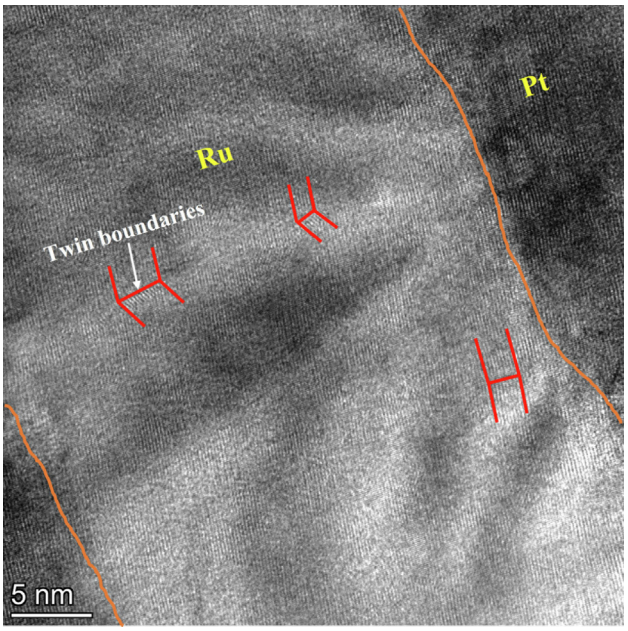

Fig. 12. HRTEM image of annealed coated sample 750–40 h.

The HAADF-STEM image and EDS mappings (Pt, Ru, Ti, C) of a FIB lamella as cut for the sample 750–40 h are exhibited in Fig. 13. At the top of the FIB sample, Pt protection layers were deposited to protect the free surface. As the damage caused by directly ion-beam Pt deposition could make the analysis of microscopic features difficult, a two-step Pt deposition approach [49], i.e., electron-beam deposition followed by ion-beam deposition, was adopted to avoid the damage. It can be observed that at some areas in the Ru–Pt multilayer coatings, the elemental Pt layers overlapped with Ru layers indicating the occurrence of diffusion owing to the thermally activated motion of Pt atoms, forming Ru-Pt solid solution. The Ru layers (Fig. 13(c)) demonstrated thermal stability even after 40 h annealing. It is worth noting that titanium did not diffuse out, which was restricted by the multilayer coating structure. It suggests the improved adherence of Ti with both multilayer coatings and the substrate. However, it is evident that after long-term annealing at 750 °C, carbon atoms from the substrate diffuse into the coating structure, which may lead to severe lattice distortion and embrittlement. This is evidenced by the crack extending from the top surface to the substrate, as shown in Fig. 13(a). The EDS mapping of C indicates that carbon atoms diffused out and likely formed a thin layer on the coating surface. In Fig. 13(b), the concentration of Pt in the electron-beam layer appeared to be lower than that in the top ion-beam deposited layer, which is caused by the interaction of carbon (layer) with the electron-beam deposited Pt.

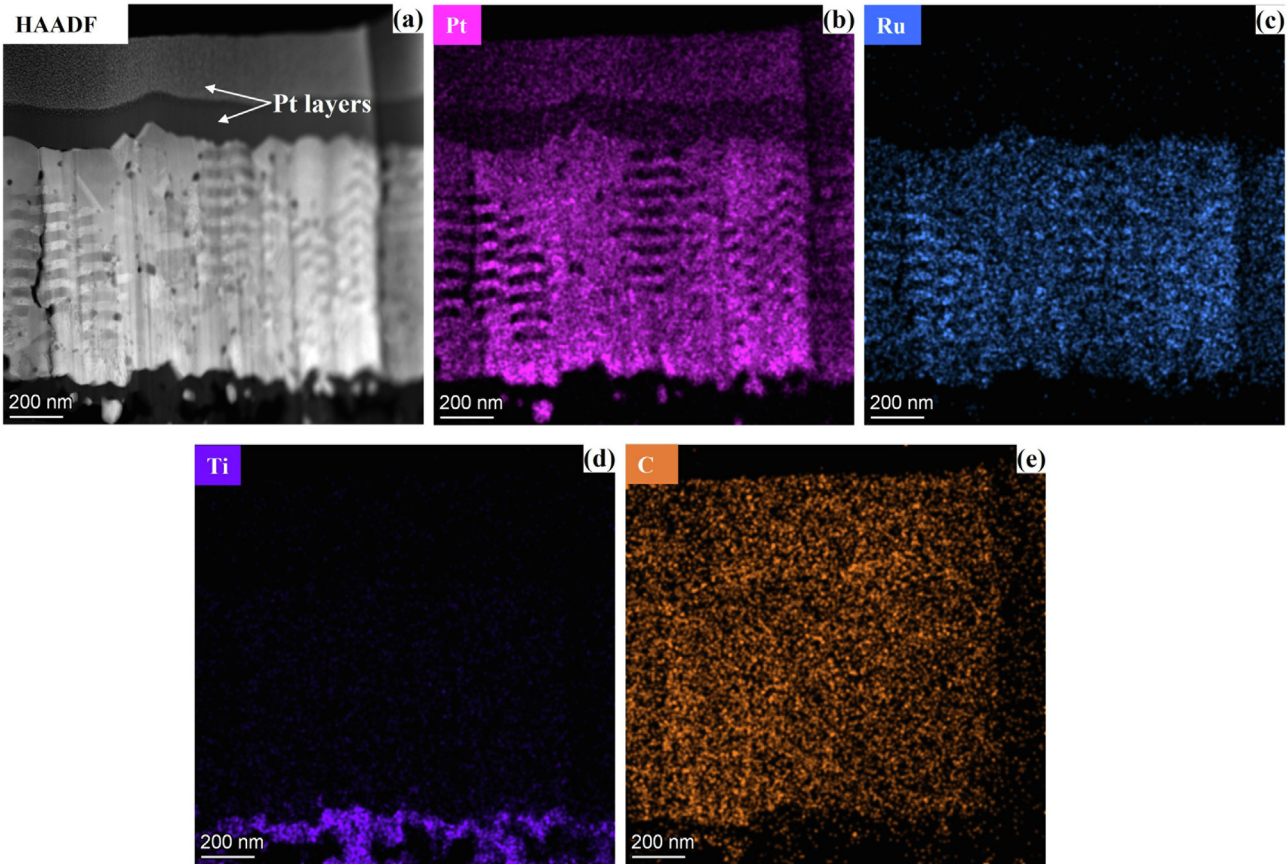

Fig. 13. Annealed coated sample (750–40 h); (a) HAADF-STEM image and EDS mappings of (b) Pt, (c) Ru, (d) Ti and (e) C.

Fig. 14 shows the HRTEM image and SAED pattern of the annealed 750–40 h coatings. In Fig. 14 (a), both layered and inter-diffused regions can be observed, which indicates the vanish of multilayer structure after the long annealing. The HRTEM image shown in Fig. 14(b) shows a magnified inter-diffused region, wherein the SAED pattern of the marked area is further exhibited in Fig. 14(c). The SAED pattern contains many bright and weak spots, indicating multiple sets of crystal lattices. It is noted that the pattern is similar to those taken from FCC/HCP interfaces (see, e.g., [50]). Because the layered structure has vanished in Fig. 14(b), the SAED pattern shown in Fig. 14(c) indicates the mixture of Pt-rich (FCC) and Ru-rich (HCP) alloys due to their interdiffusion.

3.5. Cyclic glass molding experiments

The performance of Ru-Pt coated graphite samples was further evaluated using an industrial glass molding system. Unlike laboratory experiments, the production experiments were not performed with precisely controlled process parameters. For example, N_2 flow was maintained to ensure roughly an inert atmosphere; however, the flow rate was not measured. The temperature measurement

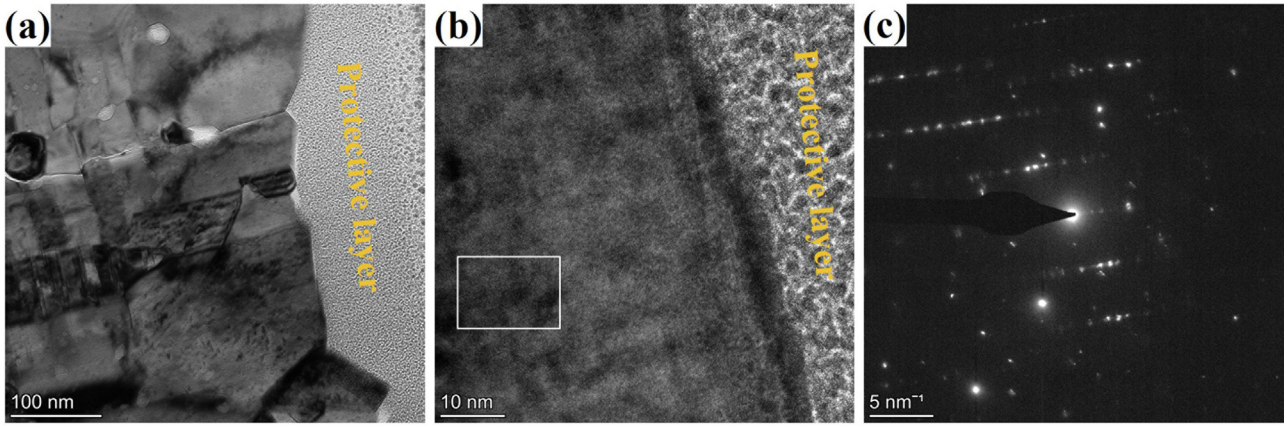

Fig. 14. Cross-sectional of 750–40 h sample; (a) TEM image, (b) HRTEM image and (c) SAED pattern of marked area in (b).

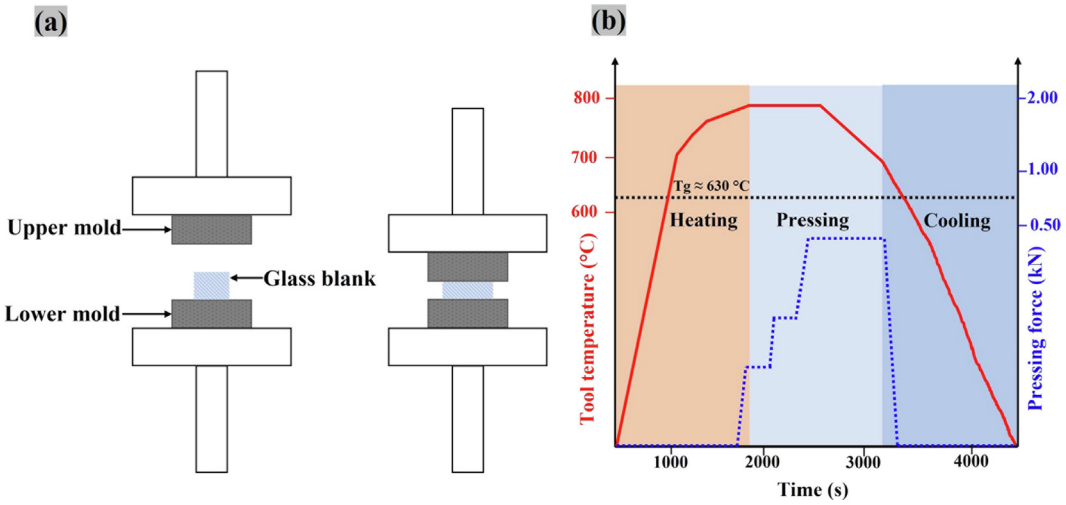

Fig. 15. Schematic of the PGM (a) testing setup and (b) typical processing cycle.

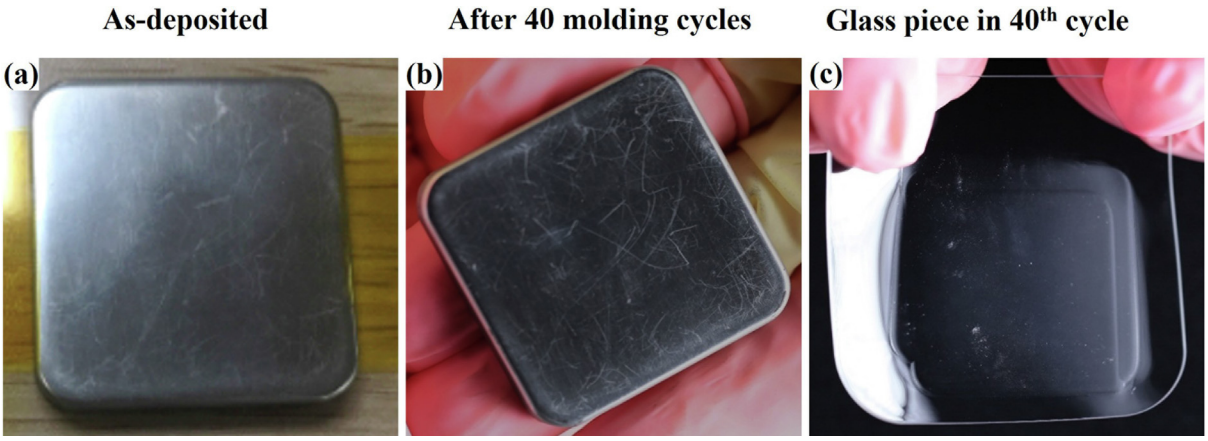

Fig. 16. Ru-Pt multilayer-coated graphite molds in the (a) as-deposited state, (b) after 40 molding cycles (c) ASG glass in 40th molding cycle.

was based on thermocouples in the heating plates contacting molding tools; the measured temperature may be different from that of glass. Fig. 15 illustrates the schematic of the industrial testing setup and the complete cycle of the molding process. A molding cycle consists of three stages: heating, pressing (molding), and cooling. In the machine, these stages were further divided into several substages. For the ASG (Corning Gorilla Glass 5) used in the test, the tool temperature in the pressing stage was 780 °C for 700 s and 700 °C for 350 s. The pressing force was ramped up to approximately 150 N for 350 s, then 600 N for 100 s, and 1850 N for 250 s at 780 °C, and maintained at 1850 N for 350 s at 700 °C. The whole molding process for one cycle took 70 min. Upon completion of one cycle, the glass piece is removed manually, and a new glass blank is inserted for the next molding round. Fig. 16 (a, b) depicts the Ru-Pt coated industrial samples (graphite substrate) before and after the molding experiments. The surface of the coated sample in the as-deposited state was rough (Ra ~ 100 nm) with a few scratches because the graphite substrate was only manually ground using sandpapers (the finest one used was 6000 grit). The coated sample was subjected to tens of molding cycles in the actual production environment. After 40 molding cycles, the coated sample was examined, and it was revealed that Ru-Pt coatings withstood pressing without any coating degradation. Even though the surfaces of the coated industrial samples were rougher than those of the laboratory ones, no macroscopic surface defect was identified after continued molding cycles. This means that the coated graphite molds for ASG glass can have a long service life in a harsh working environment. The glass piece after the 40th molding cycle was shown in Fig. 16(c), demonstrating the high anti-sticking behavior of the Ru-Pt coatings with the glass. Slight particle adherence can be detected on the surface of the glass piece, which is attributed to the environmental contamination (because graphite powders were everywhere in the machine) of the testing facility. The industrial results are consistent with the in-house performance of the multilayer coatings, suggesting that Ru-Pt multilayer coatings are a strong candidate for glass molding dies, particularly for glasses with high T_g. It should be noted that we did not suggest longer usage of the coatings because of the crack found in the 750–40 h sample (Fig. 13(a)). In the industrial test, after performing the molding for more than 40 cycles, delamination started.

4. Conclusion

In this study, Ru–Pt multilayer coatings (40 nm × 21 layers) were prepared on the graphite substrate with a 50 nm Ti interlayer by DC magnetron sputtering technique. The coatings were annealed in a rough vacuum environment with glass coverage to study its anti-stick performance for glass molding. SEM and AFM analyses demonstrated the smooth and dense surface morphology

of the as-deposited coatings, which remained almost unchanged after annealing with different time duration, indicating adequate thermal stability at the molding temperature in terms of surface characteristics. Glass sticking was not detected in SEM and XPS analyses, indicating the inertness of the coatings. Nanoindentation revealed an increase in mechanical performance with annealing time, caused by the improved coherency of Ru/Pt interfaces after short-term annealing and solid solution hardening after long-term annealing. HRTEM results are well correlated with the above observations. Most importantly, it is shown that the layered structure was preserved even after 40 h of heating at 750 °C. These results indicate that the Ru–Pt multilayer structure is a preferable candidate for the glass molding dies, especially for thermoforming high-T_g glass in the temperature range of 700–800 °C. This has been confirmed in the industry with a glass molding system.

Declaration of Competing Interest

The authors declare that they have no known competing financial interests or personal relationships that could have appeared to influence the work reported in this paper.

Acknowledgement

We gratefully acknowledge the financial support provided by the Hong Kong GRF (Grant No. 15213619) and by the industry (Ref No.: P19-0167(ME)).

Data availability

The raw data required to reproduce these findings are available from the corresponding author upon reasonable request

References

[1] H. Yumoto, H. Mimura, T. Koyama, S. Matsuyama, K. Tono, T. Togashi, Y. Inubushi, T. Sato, T. Tanaka, T. Kimura, H. Yokoyama, J. Kim, Y. Sano, Y. Hachisu, M. Yabashi, H. Ohashi, H. Ohmori, T. Ishikawa, K. Yamauchi, Focusing of X-ray free-electron laser pulses with reflective optics, Nat. Photonics 7 (1) (2013) 43–47.
[2] D.A. Atchison, Design of aspheric intraocular lenses, Ophthalmic Physiol. Opt. 11 (2) (1991) 137–146.
[3] L. Zhang, W. Liu, Precision glass molding: Toward an optimal fabrication of optical lenses, Front. Mech. Eng. 12 (1) (2017) 3–17.
[4] G. Firestone, A. Yi, Precision compression molding of glass microlenses and microlens arrays—an experimental study, Appl. Opt. 44 (29) (2005) 6115–6122.
[5] K. Kuribayashi, M. Sakai, H. Monji, M. Aoki, H. Okinaka, H. Torii, Mold for press-molding glass optical elements and a molding method using the same, Google Patents (1987).
[6] K.D. Fischbach, K. Georgiadis, F. Wang, O. Dambon, F. Klocke, Y. Chen, A.Y. Yi, Investigation of the effects of process parameters on the glass-to-mold sticking force during precision glass molding, Surf. Coat. Technol. 205 (2) (2010) 312–319.
[7] H.H. Chien, K.J. Ma, C.H. Kuo, C.B. Huo, C.L. Chao, Y.T. Chen, The effect of TaN interlayer on the performance of Pt-Ir protective coatings in glass molding process, Defect and Diffusion Forum, Trans Tech Publ, 2010, pp. 869–874.
[8] P. He, F. Wang, L. Li, K. Georgiadis, O. Dambon, F. Klocke, A.Y. Yi, Development of a low cost high precision fabrication process for glass hybrid aspherical diffractive lenses, J. Opt. 13 (8) (2011) 085703, https://doi.org/10.1088/2040-8978/13/8/085703.
[9] C.-L. Chao, C.-J. Chang, C.-C. Chen, W.-C. Chou, K.-J. Ma, in: Precision grinding of tungsten carbide mold insert for molding of sub-millimeter glass aspheric lenses, International Society for Optics and Photonics, 2013, p. 87691U.
[10] F. Klocke, O. Dambon, M. Rohwerder, F. Bernhardt, M. Friedrichs, S.V. Merzlikin, Model of coating wear degradation in precision glass molding, Int. J. Adv. Manuf. Technol. 87 (1-4) (2016) 43–49.
[11] M. Friedrichs, Z. Peng, T. Grunwald, M. Rohwerder, B. Gault, T. Bergs, PtIr protective coating system for precision glass molding tools: Design, evaluation and mechanism of degradation, Surf. Coat. Technol. 385 (2020) 125378, https://doi.org/10.1016/j.surfcoat.2020.125378.
[12] J. Wei, X. Zhu, L. Chen, J. Liu, C. Li, High quality anti-sticking coating based on multilayer structure, Surf. Coat. Technol. 362 (2019) 72–77.
[13] K.-H. Kim, K.-J. Hwang, H. Lee, S.-M. Jeong, M.-H. Lee, S.-Y. Bae, Improvement of adhesion properties of glass prepared using SiC-deposited graphite mold via low-temperature chemical vapor deposition, J. Korean Ceram. Soc. 57 (1) (2020) 112–118.
[14] J. Brand, R. Gadow, A. Killinger, Application of diamond-like carbon coatings on steel tools in the production of precision glass components, Surf. Coat. Technol. 180-181 (2004) 213–217.
[15] Y.-I. Chen, B.-L. Lin, Y.-C. Kuo, J.-C. Huang, L.-C. Chang, Y.-T. Lin, Preparation and annealing study of TaNx coatings on WC-Co substrates, Appl. Surf. Sci. 257 (15) (2011) 6741–6749.
[16] C.-H. Lin, J.-G. Duh, B.-S. Yau, Processing of chromium tungsten nitride hard coatings for glass molding, Surf. Coat. Technol. 201 (3-4) (2006) 1316–1322.
[17] C.L. Chao, C.B. Huo, W.C. Chou, T.S. Wu, K.J. Ma, C.H. Kuo, Y.T. Chen, C.W. Chao, Investigation of the interfacial reaction between optical glasses and various protective films and mold materials, Defect and Diffusion Forum, Trans Tech Publ, 2010, pp. 808–813.
[18] C.-L. Chao, C.-B. Huo, W.-C. Chou, Y.-R. Lin, K.-J. Ma, H.-H. Chien, Study on the design of precious metal based protective films for glass moulding process, Surf. Coat. Technol. 231 (2013) 567–572.
[19] S.-C. Liu, Y.-I. Chen, H.-Y. Tsai, K.-C. Lin, Y.-H. Chen, Thermal stability of Ir–Re coatings annealed in oxygen-containing atmospheres, Surf. Coat. Technol. 237 (2013) 105–111.
[20] F. Bernhardt, K. Georgiadis, L. Dolle, O. Dambon, F. Klocke, Development of a ta-C diamond-like carbon (DLC) coating by magnetron sputtering for use in precision glass molding, Materialwiss. Werkstofftech. 44 (8) (2013) 661–666.
[21] Z.W. Xie, L.P. Wang, X.F. Wang, L. Huang, Y. Lu, J.C. Yan, Influence of high temperature annealing on the structure, hardness and tribological properties of diamond-like carbon and TiAlSiCN nanocomposite coatings, Appl. Surf. Sci. 258 (3) (2011) 1206–1211.
[22] T.-N. Lin, S. Han, K.-W. Weng, C.-T. Lee, Investigation on the structural and mechanical properties of anti-sticking sputtered tungsten chromium nitride films, Thin Solid Films 529 (2013) 333–337.
[23] S. Bajt, E.J. Nelson, M.A. Wall, J. Alameda, N. Nguyen, S. Baker, J.C. Robinson, J.S. Taylor, M. Clift, A. Aquila, Oxidation resistance of Ru-capped EUV multilayers, Emerging Lithographic Technologies IX, SPIE, 2005, pp. 118-127.
[24] Y.-I. Chen, L.-C. Chang, J.-W. Lee, C.-H. Lin, Annealing and oxidation study of Mo–Ru hard coatings on tungsten carbide, Thin Solid Films 518 (1) (2009) 194–200.
[25] C. Li, R. Dai, R. Qi, X. Wu, J. Ma, Electrodeposition of Pt–Ru alloy electrocatalysts for direct methanol fuel cell, Int. J. Electrochem. Sci 12 (2017) 2485–2494.
[26] S. Hyun, O. Kraft, R.P. Vinci, Mechanical behavior of Pt and Pt–Ru solid solution alloy thin films, Acta Mater. 52 (14) (2004) 4199–4211.
[27] J. Manguele, F. Baudouin, C. Cibert, B. Domengès, V. Demange, M. Guilloux-Viry, A. Fouchet, G. Poullain, Highly textured Pt thin film grown at very low temperature using Ca 2 Nb 3 O 10 nanosheets as seed layer, SN Appl. Sci. 2 (3) (2020) 1–10.
[28] M. Sreemany, S. Sen, Effect of substrate temperature and annealing temperature on the structural, electrical and microstructural properties of thin Pt films by rf magnetron sputtering, Appl. Surf. Sci. 253 (5) (2006) 2739–2746.
[29] M. Arif, A. Sanger, P.M. Vilarinho, A. Singh, Effect of Annealing Temperature on Structural and Optical Properties of Sol-Gel-Derived ZnO Thin Films, J. Electron. Mater. 47 (7) (2018) 3678–3684.
[30] A.S. Gorzalski, C. Donley, O. Coronell, Elemental composition of membrane foulant layers using EDS, XPS, and RBS, J. Membr. Sci. 522 (2017) 31–44.
[31] E. Kusano, A. Sato, N. Kikuchi, H. Nanto, A. Kinbara, Preparation of TiC films by alternate deposition of Ti and C layers using a dual magnetron sputtering source, Surf. Coat. Technol. 120-121 (1999) 378–382.
[32] Y.-J. Chiu, C.-Y. Shen, S.-R. Jian, H.-W. Chang, J.-Y. Juang, Y.-Y. Liao, C.-L. Fan, Nanoindentation study of FePt thin films deposited by radio frequency magnetron sputtering, Nanosci. Nanotechnol. Lett. 8 (3) (2016) 260–265.
[33] K. Vinokurov, Y. Bekenstein, V. Gutkin, I. Popov, O. Millo, U. Banin, Rhodium growth on Cu 2 S nanocrystals yielding hybrid nanoscale inorganic cages and their synergistic properties, CrystEngComm 16 (40) (2014) 9506–9512.
[34] A. Obrosov, R. Gulyaev, A. Zak, M. Ratzke, M. Naveed, W. Dudzinski, S. Weiß, Chemical and morphological characterization of magnetron sputtered at different bias voltages Cr-Al-C coatings, Materials 10 (2) (2017) 156.
[35] M. Smith, L. Scudiero, J. Espinal, J.-S. McEwen, M. Garcia-Perez, Improving the deconvolution and interpretation of XPS spectra from chars by ab initio calculations, Carbon 110 (2016) 155–171.
[36] E. Ciftyürek, K. Sabolsky, E.M. Sabolsky, Platinum thin film electrodes for high-temperature chemical sensor applications, Sens. Actuators, B 181 (2013) 702–714.
[37] K. Dückers, H.P. Bonzel, D.A. Wesner, Surface core level shifts of Pt (111) measured with Y Mχ radiation (132.3 eV), Surf. Sci. 166 (1) (1986) 141–158.
[38] D. Chen, Y. Li, S. Liao, D. Su, H. Song, Y. Li, L. Yang, C. Li, Ultra-high-performance core–shell structured Ru@Pt/C catalyst prepared by a facile pulse electrochemical deposition method, Sci. Rep. 5 (1) (2015) 11604.
[39] A.S. Ramos, S. Simões, L. Maj, J. Morgiel, M.T. Vieira, Effect of Deposition Parameters on the Reactivity of Al/Ni Multilayer Thin Films, Coatings 10 (8) (2020) 721.
[40] Z.s. Czigány, G. Radnóczi, Columnar growth structure and evolution of wavy interface morphology in amorphous and polycrystalline multilayered thin films, Thin Solid Films 347 (1-2) (1999) 133–145.
[41] N.a. Liu, L. Dong, S. Jin, R. Wan, H. Gu, D. Li, Significant impact of individual surface and modulation structure on mechanical properties of NbN/NbB2 multilayers, J. Alloy. Compd. 695 (2017) 3225–3232.

[42] S.-D. Kim, S.-J. Park, J.H. Jang, J. Moon, H.-Y. Ha, C.-H. Lee, H. Park, J.-H. Shin, T.-H. Lee, Strain hardening recovery mediated by coherent precipitates in lightweight steel, Sci. Rep. 11 (1) (2021), https://doi.org/10.1038/s41598-021-93795-4.
[43] E. Shkondin, H. Alimadadi, O. Takayama, F. Jensen, A.V. Lavrinenko, Fabrication of hollow coaxial Al2O3/ZnAl2O4 high aspect ratio freestanding nanotubes based on the Kirkendall effect, J. Vacuum Sci. Technol. A Vacuum, Surf. Films 38 (1) (2020) 013402, https://doi.org/10.1116/1.5130176.
[44] J.D. Embury, J.P. Hirth, On dislocation storage and the mechanical response of fine scale microstructures, Acta Metall. Mater. 42 (6) (1994) 2051–2056.
[45] A. Misra, J.P. Hirth, R.G. Hoagland, J.D. Embury, H. Kung, Dislocation mechanisms and symmetric slip in rolled nano-scale metallic multilayers, Acta Mater. 52 (8) (2004) 2387–2394.
[46] Z. Yang, J. Wang, Coupled annealing temperature and layer thickness effect on strengthening mechanisms of Ti/Ni multilayer thin films, J. Mech. Phys. Solids 88 (2016) 72–82.
[47] W.-R. Jian, S. Xu, Y. Su, I.J. Beyerlein, Role of layer thickness and dislocation distribution in confined layer slip in nanolaminated Nb, Int. J. Plast. 152 (2022) 103239.
[48] J. Wang, X. Zhang, Twinning effects on strength and plasticity of metallic materials, MRS Bull. 41 (4) (2016) 274–281.
[49] W. Kwong, W. Zhang, Electron-beam assisted platinum deposition as a protective layer for FIB and TEM applications, ISSM 2005, IEEE International Symposium on Semiconductor Manufacturing, 2005., IEEE, 2005, pp. 469-471.
[50] B. Wei, S. Ni, Y. Liu, X. Liao, M. Song, Phase Transformation and Deformation Mechanisms in a Cold-Rolled Ti-5at.% Al Alloy, Available at SSRN 3390933 (2019).